ARTICLE

Chinese Journal of Structural Chemistry

Dual-site Doping to Enhance Oxygen Redox and Structural Stability of Li-rich Layered Oxides

Zuhao Zhang[1], Xiaoyan Xie[1], Huixian Xie[1], Xiaokai Ding[1], Jiaxiang Cui[1], Chenyu Liu[1]*, Dong Luo[1]* and Zhan Lin[1]

[1]*Guangzhou Key Laboratory of Clean Transportation Energy Chemistry, School of Chemical Engineering and Light Industry, Guangdong University of Technology, Guangzhou 510006, China*

ABSTRACT Cobalt-free Li-rich layered oxides (LLOs) such as $Li_{1.2}Mn_{0.6}Ni_{0.2}O_2$ have attracted extensive attention owing to their high specific capacity and low cost. Nonetheless, numerous problems such as continuous voltage fading and capacity decay have become stumbling blocks in its commercial application. In this study, we propose an effective dual-site doping strategy by choosing Mo as the cation and F as the anion to enhance the capacity and cycling performance. The research demonstrates that the cycling stability of LLOs enhances with the doping ratio of Mo, and their capacity increases with the doping ratio of F. It is because Mo as a pillar enhances the structural stability and F doping is conducive to the activation of Li_2MnO_3. What's more, dual-site doping also promotes the diffusion of Li^+ and reduces the internal resistance of the electrode. Due to these improvements, the 5F3M sample still maintains a discharge capacity of 190.98 mAh g^{-1} after 100 cycles at 200 mA g^{-1}, which is much higher than 165.29 mAh g^{-1} of the Pristine sample. This discovery provides a new way to develop advanced layered oxide cathodes for both Na- and Li-ion batteries.

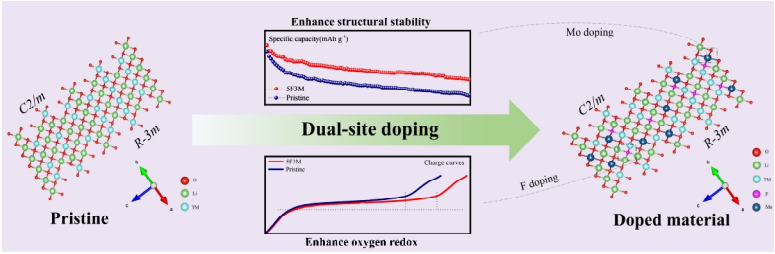

Keywords: lithium-ion battery, Li-rich layered oxides, doping, Li_2MnO_3

n INTRODUCTION

The accelerated development of the electrification trend in automotive industry has put forward higher demands for the energy density of lithium-ion batteries.[1,2] And cathode materials play a vital role in improving battery energy density. Among the present cathode material systems, the lithium-rich layered oxides (LLOs) have attracted the attention of many researchers due to their advantages of high capacity, high safety, and low cost, especially for the cobalt-free one. It is considered to be one of the most promising cathode materials of the next generation high-energy lithium-ion batteries.[3-5] Unfortunately, these cathodes suffer from structural evolution and oxygen release during cycling, resulting in serious capacity fading and voltage decay, which severely limit their practical application.[6-10]

Numerous studies have demonstrated that the structural evolution derives from the migration of transition metal (TM) ions, and the oxygen release is closely related to Li-O-Li configurations, which lowers the hybridization of O_{2p} orbital.[11-13] Both behaviors will become more serious when LLOs cathodes repeatedly undergo the deep delithiation state. To solve the above problems, researchers have proposed many improvement directions, such as surface coating,[14,15] bulk doping,[16,17] particle size control,[18] and so on. Among them, bulk doping is considered to be a relatively effective and simple strategy, which can regulate both lattice parameters and the electronic structures of materials.[19] One branch is doping at the cationic site which can serve as a pillar to retard TM migration and improve structural stability.[20] What's more, some kinds of cations are able to enhance the hybridization degree of oxygen.[20] The other one is anionic doping, which can change the electronic structure of oxygen and reduce the content of oxygen atoms with low hybridization, resulting in an increased reversibility of oxygen redox.[21] It is obvious that cation-anion doping has different effects on the crystal structure. This means that dual-site doping can combine the advantages of various doped elements to significantly improve the electrochemical performance of LLOs cathodes. However, the research and understanding on dual-site doping are not thorough enough.

In this work, we proposed a simple and effective dual-site doping strategy to enhance the capacity and cycling performance of $Li_{1.2}Mn_{0.6}Ni_{0.2}O_2$ cathodes by choosing Mo as the cation and F as the anion. Through the characterization of XRD, XPS and TEM, we confirmed that Mo ions dope into the crystal lattice and occupy the partial Li sites, which induces the formation of a spinel-like structure. This structure not only promotes the transmission of Li^+ but also acts as a pillar to enhance structural stability, thereby obtaining better cycling performance. In addition, the introduction of F element promotes the activation of the Li_2MnO_3 phase, thereby contributing more capacity. The dual-site doping with Mo and F can reduce the resistance of electrodes and promote the diffusion of Li^+, therefore resulting in a high reversible capacity, excellent rate performance and stable cycling performance. After 100 cycles at a current density of 200 mA g^{-1}, the 5F3M sample still maintains a specific discharge capacity of 190.98 mAh g^{-1}, which is much higher than the 165.29 mAh g^{-1} of the Pristine sample. Even at a current density of 400 mA g^{-1}, the 5F3M sample can still maintain a specific discharge capacity of

DOI: 10.14102/j.cnki.0254-5861.2022-0066

about 170 mAh g^{-1}, while for the Pristine sample it is only about 144 mAh g^{-1}. This work provides a new strategy for the design of advanced LLOs cathode materials for high-energy Li-ion batteries.

n RESULTS AND DISCUSSION

X-ray powder diffraction (XRD) is employed to confirm the information about the crystal structures of as-prepared materials. As displayed in Figure 1a, all patterns show a typical crystal structure of LLOs cathode material. The diffraction peaks of the as-prepared materials are indexed to a hexagonal α-$NaFeO_2$ structure, which corresponds to $LiMO_2$ (M = Ni and Mn) phase (space group: *R-3m*). Some weak peaks appear in the range of 20–25 degrees, which are indexed to the Li_2MnO_3 phase (space group: *C2/m*).[22] A good split of the (006)/(012) and (018)/(110) peaks demonstrates that all samples have formed a highly ordered layered structure.[23] Compared with the Pristine sample, no other impurity peaks can be detected in the dual-site doping materials, which indicates that the treatment of NH_4F and $(NH_4)_2MoO_4$ has very little effect on the material structure. Meanwhile, Raman spectroscopy is used to analyze the surface structure. As shown in Figure S1, the band near 423 cm^{-1} is attributed to the monoclinic Li_2MnO_3 phase, and the two broad bands near 490 and 610 cm^{-1} belong to the E_g and A_{1g} vibrations of the layered structure, respectively.[24,25] All Raman spectra indicate that the as-prepared materials possess a structure with two-phase domain, which is consistent with the XRD results. This further proves that the synthesized samples are LLOs cathode materials.

The morphology of the Pristine sample and dual-site doping samples was characterized by SEM, as shown in Figures 1e–h, S2, and S3. It can be found that all the samples are assembled spheres densely packed with primary nanoparticles. And there is no obvious difference between the morphology of all materials. This means that the dual-site doping does not change the morphology of the samples after treatment. At the same time, energy dispersive X-ray (EDX) spectroscopy elemental mapping was used to confirm the distribution of each element on the surface of the sample. As exhibited in Figures 1i–l, the Mn, Ni, F, and Mo elements distribute evenly in the dual-site doping sample, and there is no obvious visible clustering phenomenon. In addition, the mapping also indicates Mo and F elements exist in the treated samples.

Since SEM can only provide the distribution of elements on the surface, it cannot investigate the effects of the treated process on the crystal lattice, element valence, etc. Therefore, the further research will focus on the Pristine and 5F3M samples. Figure 2a and b displays the refined XRD patterns. The detailed structure information is displayed in Table S1, and the corresponding results are shown in Table 1 and S2. Compared with the Pristine sample, lattice parameters a and c of the *R-3m* and *C/2m* phases for the 5F3M sample are both increased. This provides direct evidence that Mo ions enter the crystal lattice and cause the expansion of the Li layer.[26] Meanwhile, c/a values of the *R-3m* phase are more than 4.9, further confirming that the material has a highly ordered layered structure.[27] The larger I(003)/I(104) value

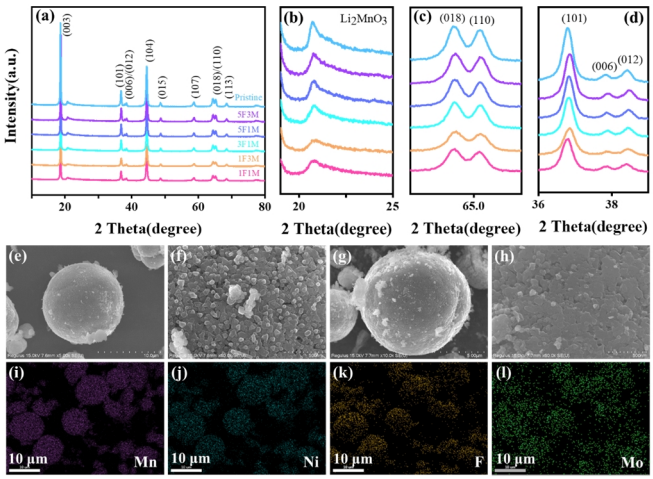

Figure 1. (a) XRD patterns of the Pristine and dual-site doping samples. The magnified patterns of (b) 19–25 degrees, (c) 36–39 degrees, and (d) 63–66 degrees. SEM images of (e, f) Pristine and (g, h) 5F3M material, and (i–l) the elemental mapping of Mn, Ni, F, and Mo in the 5F3M sample.

also indicates that the material has a more ordered structure.[28] The Rietveld refinement results demonstrate that Mo ions successfully dope into the crystal lattice, and lead to an expansion in lattice parameters.

Valence states of each element and the chemical environment of F were determined by XPS analysis. Figures 2c–h shows the XPS spectrum of the O 1*s*, Mn 3*s*, Mo 3*d*, and F 1*s* orbitals of the Pristine and 5F3M samples. The detected characteristic peaks of F and Mo in XPS further prove that the treated samples contain F and Mo elements, which are mutually supportive with the results of EDX mentioned above. As shown in Figures 2c and d, the O 1*s* spectra of the two samples are similar, and can be obviously divided into three peaks. The strong peak at ~529.4 eV corresponds to the lattice oxygen of metal-oxygen bonds, the peak at ~531 eV is classified as various adsorbed species on the particle surface, and the weak peak at ~533 eV can be attributed to hydroxyl-like species.[29-32] This indicates that the oxygen chemical environment of the two samples is consistent.

Moreover, the valence state of TM ions was also detected. As shown in Figure S4, the binding energy of Ni 2*p*3/2 is located at about 854.12 eV, which is very close to Ni 2*p*3/2 (854.2 eV) in NiO. This shows that the Ni valence state of the two samples is +2. In the Mn2*p* spectrum, the Mn 2*p*3/2 and Mn 2*p*1/2 of the two samples are about 642.1 and 653.60 eV, respectively, indicating the presence of Mn^{4+}. However, the binding energy value of Mn 2*p*3/2 is very close to the values of Mn^{4+} (642.2–642.8 eV) and

Table 1. Rietveld Refinement Results for Pristine and 5F3M Samples

Phase	Sample	Lattice constant		c/a
		a	c	
R-3m	Pristine	2.8586(1)	14.2466(4)	4.9837
	5F3M	2.8608(1)	14.2539(4)	4.9824
C/2m	Pristine	4.928(2)	5.041(2)	/
	5F3M	4.961(1)	5.0628(9)	/

DOI: 10.14102/j.cnki.0254-5861.2022-0066

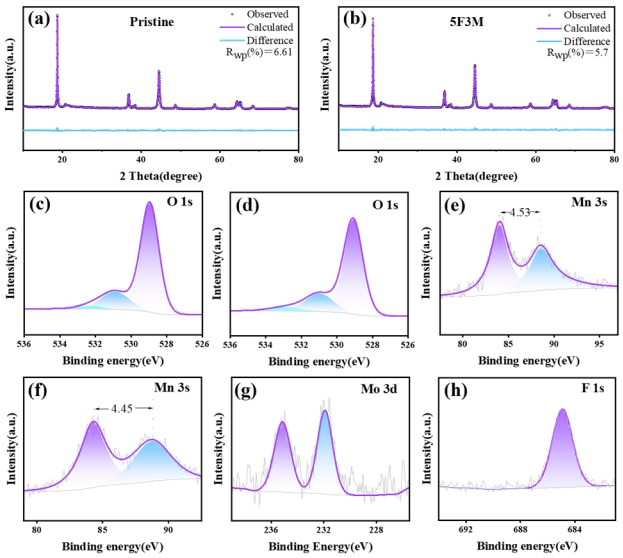

Figure 2. Rietveld refinement patterns for (a) Pristine and (b) 5F3M sample. XPS spectra: (c, d) O 1*s* and (e, f) Mn 3*s* of the Pristine and 5F3M samples; (g) Mo 3*d* and (h) F 1*s* of the 5F3M sample.

Mn^{3+} (641.7–642.2 eV).[33] Herein, the energy spectrum of Mn 3*s* is further employed to determine the valence state of Mn, as shown in Figures 2e and f. The splitting energies of the Pristine and 5F3M samples are 4.53 and 4.45 eV, respectively. It confirms that the valence state of Mn in the two samples is +4.[34,35]

In the F 1*s* spectrum, the binding energy is located at 684.93 eV, indicating the formation of M–F (M = Mn and Ni) bond, which means that F ions have successfully entered the material lattice.[36] The 3*d*5/2 and 3*d*3/2 peaks of the Mo 3*d* spectrum at 231.92 and 235.14 eV indicate that Mo is introduced into the bulk phase in the form of a valence state of +6.[37] Mo is already in the highest valence state, which means that it does not have electrochemical activity. Therefore, too much doping ratio of Mo ions may adversely affect the capacity of cathodes. In short, the results of XPS demonstrate that F has successfully entered the crystal lattice of the material, and the introduction of F and Mo does not affect the oxidation valence of transition metal ions.

The effects of dual-site doping on crystal structure were further investigated by TEM. Figures 3 and S5 show the TEM images of the Pristine and 5F3M samples, which once again proves that the synthesized samples have a morphology of assembled microspheres. As exhibited in Figure 3, clear lattice fringes can be observed. All the enlarged regions exhibit a wide lattice fringe with a lattice spacing about 0.47–0.48 nm. It corresponds to the (003) crystal plane of $LiMO_2$ structure or (001) facet of Li_2MnO_3 component.[38,39] This also indicates that the dual-site doping does not change the bulk structure, which is consistent with the results of XRD. The enlarged regions II and IV are the edges of the Pristine and 5F3M samples. Obviously, a short lattice fringe emerges on the surface area of the 5F3M sample, while it cannot be observed in the corresponding region of the Pristine sample. Since the brighter the dots, the heavier the atomic mass, the bright lattice fringe is the TM layer and the dark one belongs to the Li layer.[40] Therefore, the short lattice fringes on the surface

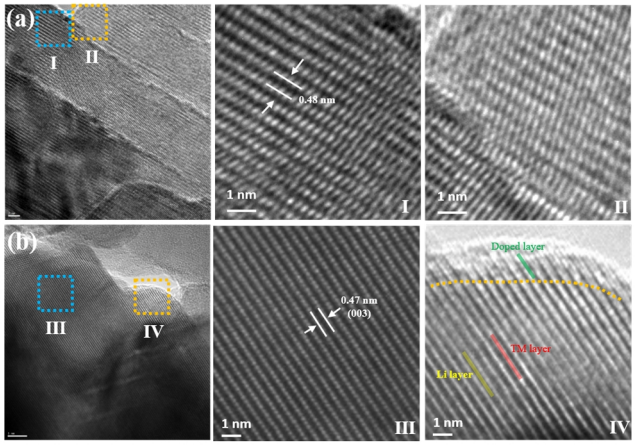

Figure 3. TEM images of (a) Pristine and (b) 5F3M material. I-IV are the corresponding enlarged region of each material.

area are due to some Mo ions occupying partial Li site in the Li layer. Note that bright spots are only observed in the Li layer on the surface area, but disappear in the interior. This indicates that doping induces surface structure evolution. Some doped elements enter the surface Li layer and lead to the generation of a spinel-like structure. This is conducive to the transmission of Li^+.[42,43] Meanwhile, the spinel-like structure also plays a role as a pillar, which will mitigate the undesired interface reaction and improve the surface structural stability.[44,45]

The electrochemical properties of the samples were tested in the voltage range of 2.0–4.8 V. The initial charge and discharge curves of the samples at a current density of 0.1 C are shown in Figure 4a. All materials show a characteristic profile of LLOs cathode materials. The voltage ramp below 4.5 V corresponds to the extraction of Li^+ from the $LiMO_2$ phase, which is reflected in the dQ/dV curve as an oxidation peak located at 3.75 to 4.1 V.[46] The voltage plateau beyond 4.5 V is related to the activation process of the Li_2MnO_3 phase, which is reflected as the redox peaks at 4.5 and 3.3 V in the dQ/dV curve.[47] Note that the voltage plateau of the dual-site doping samples is longer than that of the Pristine sample. It suggests the capacity provided by the Li_2MnO_3 component in each sample is not consistent. To this end, the capacity contribution of the two phases in each sample during the first charging process was quantified in terms of the method shown in Figure S6, and the corresponding data are listed in Table S2.[48] Compared with the Pristine sample, the capacity contribution of the Li_2MnO_3 phase for the 5F3M sample (190.9 mAh g^{-1}) is increased by 37 mAh g^{-1}. In addition, the initial Coulombic efficiency of 5F3M sample is 78.42%, which is also higher than that of the Pristine sample (76.69%), resulting in a significant increase in reversible discharge capacity of the first cycle. These indicate that the activation of the Li_2MnO_3 phase becomes easier after dual-site doping.

Figure 4c shows the cycle performance of the samples at a current density of 1 C. Compared with the 1F1M and 1F3M samples, the cycle performance improves with increasing the doping ratio of Mo. This phenomenon was further confirmed by the 5F1M and 5F3M samples. It is because Mo as a pillar enhances the structural stability, thereby obtaining an excellent

DOI: 10.14102/j.cnki.0254-5861.2022-0066

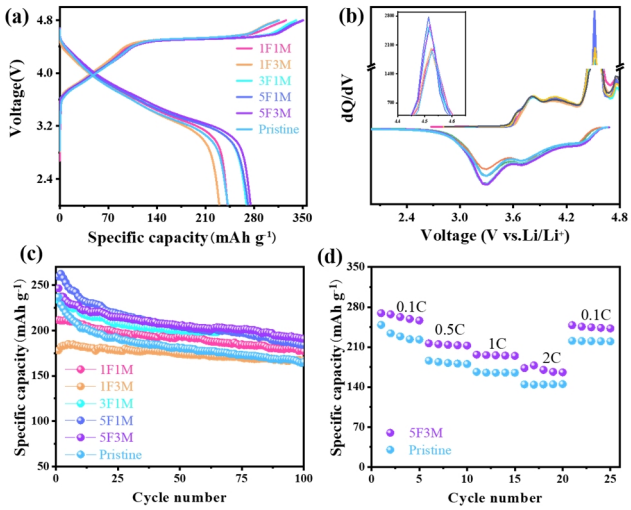

Figure 4. (a) Initial charge-discharge profiles of Pristine and dual-site doping materials at 0.1 C and (b) corresponding dQ/dV curves. (c) Cycle performance at 1 C of Pristine and dual-site doping samples. (d) Rate performance of Pristine and 5F3M sample.

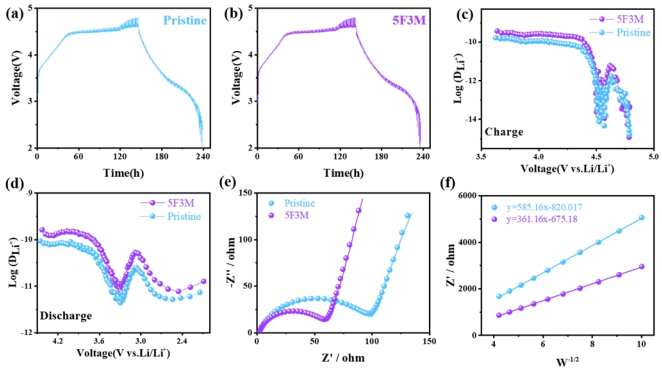

Figure 5. GITT curves of (a–b) the Pristine and 5F3M samples; Diffusion coefficients of Li^+ during the (c) charge and (d) discharge process. (e) Nyquist plots of the Pristine and 5F3M samples and (f) the plots of Z' versus $\omega^{-1/2}$.

cycle performance. This significant role of cationic doping is also mentioned in the previous reports of Zang et al.[49] However, the discharge capacity of the 1F3M sample is very low due to the electrochemical inertia of Mo^{6+} ions. Too much doping ratio leads to a reduction of discharge capacity. It is a contradiction between discharge capacity and cycling stability, which is very common in improving the electrochemical performance of cathodes by bulk doping.

When enhancing the doping ratio of F from 1% to 5% (the 5F3M sample), the discharge capacity has an obvious improvement. This can be attributed to the fact that F doping is conducive to the activation of Li_2MnO_3, which can be directly observed in the initial charge process (Figure 4a). This result is also supported by the research of Song et al., in which they have demonstrated that F doping improves the efficiency of the Li_2MnO_3-like component and inhibits irreversibility.[50] Owing to the synergistic action of F and Mo, the 5F3M sample delivers the best capacity and cycle performance among all dual-site doping samples. After 100 cycles, it still maintains a discharge capacity of 190.98 mAh g^{-1}, which is much higher than 165.29 mAh g^{-1} of the Pristine sample. By comparing with the specific capacity and cycle performance of other reported work in Table S3, our work is at an intermediate level and has a higher specific capacity. Meanwhile, the rate performance of the two samples was tested and the results are shown in Figure 4d. It can be clearly seen that the 5F3M sample has better rate performance than the Pristine sample. Even at a current density of 400 mA g^{-1} (2C), it can still maintain a specific discharge capacity of about 170 mAh g^{-1}, while the Pristine sample is only about 144 mAh g^{-1}. This suggests that the synergistic effect of F and Mo also enhances the diffusion kinetics of Li^+.

In order to confirm the promoting effect of dual-site doping on the electrode kinetics of cathodes, GITT was used to analyze the lithium-ion diffusion coefficient (D_{Li^+}) of the Pristine and 5F3M samples. Figures 5a and b show the GITT curves at a current density of 20 mA g^{-1} between 2.0 to 4.8 V for the initial charge and discharge process. The D_{Li^+} in this process is calculated by the following formula:[51]

$$D_{Li^+} = \frac{4}{\pi}\left(\frac{m_B V_M}{M_B S}\right)^2 \left(\frac{\Delta E_s}{\tau d E_x / d\sqrt{\tau}}\right)^2 \quad (\tau \ll L^2 / D_{Li^+})$$

Since the applied current is very small and the relaxation time τ is very short, we believe that E_x and τ has a linear relationship, so the above formula can be simplified as:[51]

$$D_{Li^+} = \frac{4}{\pi}\left(\frac{m_B V_M}{M_B S}\right)^2 \left(\frac{\Delta E_s}{\Delta E_t}\right)^2$$

In this formula, m_B and M_B are the mass and relative molecular mass of $Li_{1.2}Mn_{0.6}Ni_{0.2}O_2$, respectively. V_M is the molar volume derived from crystallographic data, S is the area of the electrode, ΔE_s is the voltage change caused by the pulse, and ΔE_t is the voltage change resulting from the constant current charging and discharging. Figures 5c and d show the D_{Li^+} under different voltages which are calculated according to the above formula. During the entire charging process, D_{Li^+} for the two cathodes is between 10^{-9} and $10^{-15.5}$ cm^2 s^{-1}, and the discharge process is between $10^{-11.5}$ and $10^{-9.5}$ cm^2 s^{-1}. Obviously, the D_{Li^+} of the 5F3M sample is always larger than that of the Pristine sample during the initial cycle. This is due to the dual-site doping which promotes the transmission of Li^+ and results in better lithium-ion diffusion kinetics. Therefore, the rate performance of 5F3M sample is better than that of Pristine in Figure 4d.

EIS was performed to further verify the effect of dual-site doping on lithium-ion diffusion kinetics. The Nyquist plots of all samples are shown in Figure S7. It can be clearly seen that the impedance of all samples is in the order of 1F3M > 1F1M > Pristine > 3F1M > 5F1M > 5F3M, which is consistent with their discharge capacity. For comparison, the Nyquist plots of the 5F3M sample and Pristine sample were fitted and the D_{Li^+} were calculated. As shown in Figure 5e, the solid line is the test data, the point is the fitting result and the illustration shows the fitted equivalent circuit diagram. It can be clearly seen that the total resistance of the 5F3M sample is smaller than that of the Pristine sample. This

DOI: 10.14102/j.cnki.0254-5861.2022-0066

means dual-site doping can improve the conductivity of cathode materials. In addition, the D_{Li^+} is also calculated by the following formula:[52]

$$D_{Li^+} = \frac{R^2T^2}{2A^2F^4n^4C^2\sigma^2}$$

Among them, R is the ideal gas constant, T is the absolute temperature during the test, A is the area of the electrode, F is the Faraday constant, n is the number of electrons lost by oxidation once per unit molecule, and C is the concentration of Li^+ in the material. σ is the Weber coefficient, which is the slope of Z' to $\omega^{-1/2}$ in Figure 5f. After calculation, the $D_{Li^+}$of the Pristine and 5F3M samples are 4.46×10^{-20} and 1.17×10^{-19} cm^2 s^{-1}, respectively. It is obvious that the 5F3M sample has greater lithium-ion diffusion kinetics, which is consistent with the data of GITT mentioned above. This suggests that the dual-site doping with Mo and F can reduce the resistance of electrodes and promote the diffusion of Li^+, therefore resulting in a high reversible capacity, excellent rate performance and stable cycling performance.

n CONCLUSION

In summary, an effective dual-site doping strategy by choosing Mo as the cation and F as the anion was proposed to improve the capacity and cycle performance of $Li_{1.2}Mn_{0.6}Ni_{0.2}O_2$ cathodes. Combined with the Rietveld refinement of XRD, XPS, and TEM characterization, we confirmed that some Mo ions successfully dope into the crystal lattice and occupy the partial Li sites, forming a spinel-like structure, which enhances the structural stability of the material and expands the diffusion rate of Li^+. In addition, the introduction of F element promotes the activation of Li_2MnO_3 phase. Compared with Pristine sample, the capacity contribution of Li_2MnO_3 phase for the 5F3M sample (190.9 mAh g^{-1}) is increased by 37 mAh g^{-1}. Due to the synergistic action of F and Mo, the 5F3M sample still maintains a specific discharge capacity of 190.98 mAh g^{-1} after 100 cycles, which is much higher than 165.29 mAh g^{-1} of the Pristine sample, suggesting excellent cycling stability. Even at a current density of 400 mA g^{-1}, 5F3M sample can still maintain a specific discharge capacity of about 170 mAh g^{-1}, while the Pristine sample is only about 144 mAh g^{-1}. Therefore, the excellent capacity and cycling performance after dual-site doping suggest that this work provides a new scheme to prepare advanced cathode materials for the next-generation of high-energy Li-ion batteries.

n EXPERIMENTAL

Preparation of Material. The Mo and F dual-site doping LLOs cathode materials ($Li_{1.2}Mn_{0.6}Ni_{0.2}O_2$) were prepared by the molten salt method. Carbonate precursor ($Mn_{0.75}Ni_{0.25}CO_3$) was purchased from Haian Zhichuan Battery Material Technology Co., Ltd. Li_2CO_3, NaCl, and KCl were obtained from Shanghai Aladdin Biochemical Technology Co., Ltd. NH_4F and $(NH_4)_2MoO_4$ were provided by Shanghai Macklin Biochemical Technology Co., Ltd. The preparation process of the material is as follows. First, a certain amount of the precursor, NH_4F (5 wt%) and $(NH_4)_2MoO_4$ (3 mol%) was uniformly ground in an agate mortar. Then the mixture was transferred to the polytetrafluoroethylene lining of the hydrothermal reactor for reacting at 180 °C for 12 hours. After mixing with Li_2CO_3, NaCl, and KCl, they were calcined in a muffle furnace at 830 °C for 12 hours under an air atmosphere. Finally, the sample was obtained after washing, filtering, and drying, named 5F3M. The same steps were used to get different doped ratio samples, named 1F1M, 1F3M, 3F1M, and 5F1M, respectively. For comparison, an undoped sample was prepared under the same process conditions except for the lack of NH_4F and $(NH_4)_2MoO_4$ treated procedure, named Pristine.

Characterization of Samples. X-ray diffraction (XRD) with a Cu-Kα radiation source (λ = 1.54059 Å, 40 kV, 50.0 mA) was applied to characterize the structures of all materials, scanned over a range of 10–80° at a scan rate of 2 °/min. The surface morphology, element distribution, and crystal structure of the materials were analyzed by field emission scanning electron microscope (SEM) equipped with the energy dispersive X-ray spectrometer (EDS), and transmission electron microscope (TEM). X-ray photoelectron spectroscopy (XPS) was used to verify the valence states of the elements, and the phase compositions were detected by a Raman microscope.

Electrochemical Test of Samples. The positive electrode is composed of 80 wt% as-prepared material, 10 wt% polyvinylidene fluoride (PVDF), and 10 wt% N-methyl pyrrolidinone (NMP). The negative electrode is metallic Li, the microporous polypropylene membrane serves as the separator, and the electrolyte consists of 1 M $LiPF_6$ dissolved in ethylene carbonate (EC):ethyl methyl carbonate (EMC):dimethyl carbonate (DMC) (1:1:1 by volume). All the materials are assembled as a CR2016 coin cell battery in the glove box, and the electrochemical performance of materials is tested by NEWARE battery test system under the voltage window of 2.0 to 4.8 V. Among them, the loading amount of active material is between 1.3 and 1.62 mg/cm^2. For the galvanostatic intermittent titration technique (GITT) measurement, the current density is 20 mA g^{-1}, and the current pulse and relaxation time is 10 and 60 min, respectively. The electrochemical impedance spectroscopy (EIS) test is performed in the frequency range of 10^{-2}–10^5 Hz.

n ACKNOWLEDGEMENTS

This work was financially supported by the National Natural Science Foundation of China (52004070 and 51874104) and the National Key R&D Program of China (2011YFB0700600).

n AUTHOR INFORMATION

Corresponding author. Emails: cy.liu@gdut.edu.cn and luodong@gdut.edu.cn

n COMPETING INTERESTS

The authors declare no competing interests.

n ADDITIONAL INFORMATION

Supplementary information is available for this paper at http://manu30.magtech.com.cn/jghx/EN/10.14102/j.cnki.0254-5861.2022-0066

DOI: 10.14102/j.cnki.0254-5861.2022-0066

For submission: https://mc03.manuscriptcentral.com/cjsc

n REFERENCES

(1) Andre, D.; Kim, S. J.; Lamp, P.; Lux, S. F.; Maglia, F.; Paschos, O.; Stiaszny, B. Future generations of cathode materials: an automotive industry perspective. *J. Mater. Chem. A* **2015**, 3, 6709–6732.

(2) Lin, Z.; Liu, T. F.; Ai, X. P.; Liang, C. D. Aligning academia and industry for unified battery performance metrics. *Nat. Commun.* **2018**, 9, 1–5.

(3) Manthiram, A. A reflection on lithium-ion battery cathode chemistry. *Nat. Commun*. **2020**, 11, 1–9.

(4) Zheng, Z.; Wang, M. Y.; Yang, L. Y.; Hu, Z. X.; Chen, Z. F.; Pan, F. Thermodynamically revealing the essence of order and disorder structures in layered cathode materials. *Chin. J. Struct. Chem.* **2019**, 38, 2020–2026.

(5) Liu, T. C.; Pan, F.; Khalil, A. Prospect and reality of concentration gradient cathode of lithium-ion batteries. *Chin. J. Struct. Chem.* **2020**, 39, 11–15.

(6) Lu, Z. H.; Dahn, J. R. Understanding the anomalous capacity of Li/Li[$Ni_xLi_{(1/3-2x/3)}Mn_{(2/3-x/3)}$]$O_2$ cells using in situ X-ray diffraction and electrochemical studies. *J. Electrochem. Soc.* **2002**, 149, A815–A822.

(7) Song, B. H.; Liu, Z. W.; Lai, M. O.; Lu, L. Structural evolution and the capacity fade mechanism upon long-term cycling in Li-rich cathode material. *Phys. Chem. Chem. Phys.* **2012**, 14, 12875–12883.

(8) Liu, W.; Oh, P.; Liu, X. E.; Myeong, S.; Cho, W.; Cho, J. Countering voltage decay and capacity fading of lithium-rich cathode material at 60 °C by hybrid surface protection layers. *Adv. Energy Mater.* **2015**, 5, 1500274.

(9) Yin, Z. W.; Li, J. T.; Huang, L.; Pan, F.; Sun, S. G. High-capacity Li-rich Mn-based cathodes for lithium-ion batteries. *Chin. J. Struct. Chem.* **2020**, 39, 20–25.

(10) Yu, Y. M.; Liu, J. J.; Qi, R.; Zuo, C. J.; Zhao, W. G.; Lu, J. L.; Zhang, M. J.; Pan, F. Interface-reconstruction forming bifunctional (Li_xTM_{1-x})O rock-salt shell for enhanced cyclability in Li-rich layered oxide. *Chin. J. Struct. Chem.* **2020**, 39, 1363–1371.

(11) Seo, D. H.; Lee, J.; Urban, A.; Malik, R.; Kang, S.; Ceder, G. The structural and chemical origin of the oxygen redox activity in layered and cation-disordered Li-excess cathode materials. *Nat. Chem.* **2016**, 8, 692–697.

(12) Zhu, Z.; Yu, D. W.; Yang, Y.; Su, C.; Huang, Y. M.; Dong, Y. H.; Waluyo, I.; Wang, B.; Hunt, A.; Yao, X. H.; Lee, J.; Xue, W. J.; Li, J. Gradient Li-rich oxide cathode particles immunized against oxygen release by a molten salt treatment. *Nat. Energy* **2019**, 4, 1049–1058.

(13) Yu, H. J.; So, Y. G.; Ren, Y.; Wu, T. H.; Guo, G. C.; Xiao, R. J.; Lu, J.; Li, H.; Yang, Y. B.; Zhou, H. S.; Wang, R. Z.; Amine, K.; Ikuhara, Y. Temperature-sensitive structure evolution of lithium-manganese-rich layered oxides for lithium-ion batteries. *J. Am. Chem. Soc.* **2018**, 140, 15279–15289.

(14) Kim, S. Y.; Park, C. S.; Hosseini, S.; Lampert, J.; Kim, Y. J.; Nazar, L. F. Inhibiting oxygen release from Li-rich, Mn-rich layered oxides at the surface with a solution processable oxygen scavenger polymer. *Adv. Energy Mater.* **2021**, 11, 2100552.

(15) Peng, J. M.; Li, Y.; Chen, Z. Q.; Liang, G. M.; Hu, S. J.; Zhou, T. F.; Zheng, F. H.; Pan, Q. C.; Wang, H. Q.; Li, Q. Y.; Liu, J. W.; Guo, Z. P. Phase compatible $NiFe_2O_4$ coating tunes oxygen redox in Li-rich layered oxide. *ACS Nano* **2021**, 15, 11607–11618.

(16) Xu, C. Y.; Li, J. L.; Sun, J.; Zhang, W. Z.; Ji, B. M. Li-rich layered oxide single crystal with Na doping as a high-performance cathode for Li-ion batteries. *J. Alloys Compd.* **2021**, 895, 162613.

(17) Singh, A. N.; Kim, M. H.; Meena, A.; Wi, T. U.; Lee, H. W.; Kim, K. S. Na/Al co-doped layered cathode with defects as bifunctional electrocatalyst for high-performance Li-ion battery and oxygen evolution reaction. *Small* **2021**, 17, 2005605.

(18) Liu, J. H.; Chen, H. Y.; Xie, J. N.; Sun, Z. Q.; Wu, N. N.; Wu, B. R. Electrochemical performance studies of Li-rich cathode materials with different primary particle sizes. *J. Power Sources* **2014**, 251, 208–214.

(19) Zhang, B. K.; Tan, R.; Yang, L. Y.; Zheng, J. X.; Zhang, K. C.; Mo, S. J.; Lin, Z.; Pan, F. Mechanisms and properties of ion-transport in inorganic solid electrolytes. *Energy Storage Mater.* **2018**, 10, 139–159.

(20) Liu, S.; Liu, Z. P.; Shen, X.; Wang, X. L.; Liao, S. C.; Yu, R. C.; Wang, Z. X.; Hu, Z. W.; Chen, C. T.; Yu, X. Q.; Yang, X. Q.; Chen, L. Q. Li–Ti cation mixing enhanced structural and performance stability of Li-rich layered oxide. *Adv. Energy Mater.* **2019**, 9, 1901530.

(21) Wang, T. D.; Zhang, C. X.; Li, S. W.; Shen, X.; Zhou, L. J.; Huang, Q.; Liang, C. P.; Wang, Z. X.; Wang, X. F.; Wei, W. F. Regulating anion redox and cation migration to enhance the structural stability of Li-rich layered oxides. *ACS Appl. Mater. Interfaces* **2021**, 13, 12159–12168.

(22) Julien, C.; Massot, M. Lattice vibrations of materials for lithium rechargeable batteries I. Lithium manganese oxide spinel. *Mater. Sci. Eng. B* **2003**, 97, 217–230.

(23) Zhao, S. Y.; Zhu, Y. T.; Qian, Y. C.; Wang, N. N.; Zhao, M.; Yao, J. L.; Xu, Y. H. Annealing effects of TiO_2 coating on cycling performance of Ni-rich cathode material $LiNi_{0.8}Co_{0.1}Mn_{0.1}O_2$ for lithium-ion battery. *Mater. Lett.* **2020**, 265, 127418.

(24) Amalraj, S. F.; Burlaka, L.; Julien, C. M.; Mauger, A.; Kovacheva, D.; Talianker, M.; Markovsky, B.; Aurbach, D. Phase transitions in Li_2MnO_3 electrodes at various states-of-charge. *Electrochim. Acta* **2014**, 123, 395–404.

(25) Inaba, M.; Iriyama, Y.; Ogumi, Z.; Todzuka, Y.; Tasaka, A. Raman study of layered rock-salt $LiCoO_2$ and its electrochemical lithium deintercalation. *J. Raman Spectrosc.* **1997**, 28, 613–617.

(26) Xu, Y. B.; Zhang, M. X.; Yi, L.; Liang, K. Fe^{3+} and PO_4^{3-} co-doped Li-rich $Li_{1.20}Mn_{0.56}Ni_{0.16}Co_{0.08}O_2$ as cathode with outstanding structural stability for lithium-ion battery. *J. Alloys Compd.* **2021**, 865, 158899.

(27) Shaju, K.; Rao, G. S.; Chowdari, B. Performance of layered $Li(Ni_{1/3}Co_{1/3}Mn_{1/3})O_2$ as cathode for Li-ion batteries. *Electrochim. Acta* **2002**, 48, 145–151.

(28) Shen, C. H.; Wang, Q.; Fu, F.; Huang, L.; Lin, Z.; Shen, S. Y.; Su, H.; Zheng, X. M.; Xu, B. B.; Li, J. T.; Sun, S. G. Facile synthesis of the Li-rich layered oxide $Li_{1.23}Ni_{0.09}Co_{0.12}Mn_{0.56}O_2$ with superior lithium storage performance and new insights into structural transformation of the layered oxide material during charge-discharge cycle: in situ XRD characterization. *ACS Appl. Mater. Interfaces* **2014**, 6, 5516–5524.

(29) Rong, X. H.; Liu, J.; Hu, E. Y.; Liu, Y. J.; Wang, Y.; Wu, J. P.; Yu, X. Q.; Page, K.; Hu, Y. S.; Yang, W. L.; Li, H.; Yang, X. Q.; Chen, L. Q.; Huang. X. J. Structure-induced reversible anionic redox activity in Na layered oxide cathode. *Joule* **2018**, 2, 125–140.

(30) Foix, D.; Sathiya, M.; McCalla, E.; Tarascon, J. M.; Gonbeau, D. X-ray photoemission spectroscopy study of cationic and anionic redox processes in high-capacity Li-ion battery layered-oxide electrodes. *J. Phys. Chem. C* **2016**, 120, 862–874.

(31) Yi, T. F.; Shi, L. N.; Han, X.; Wang, F. F.; Zhu, Y. R.; Xie, Y. Approaching high-performance lithium storage materials by constructing

DOI: 10.14102/j.cnki.0254-5861.2022-0066

hierarchical $CoNiO_2$@CeO_2 nanosheets. *Energy Environ. Mater.* **2021**, 4, 586–595.

(32) Yi, T. F.; Qiu, L. Y.; Mei, J.; Qi, S. Y.; Cui, P.; Luo, S. H.; Zhu, Y. R.; Xie, Y.; He, Y. B. Porous spherical NiO@$NiMoO_4$@PPy nanoarchitectures as advanced electrochemical pseudocapacitor materials. *Sci. Bull.* **2020**, 65, 546–556.

(33) Ivanova, S.; Zhecheva, E.; Stoyanova, R.; Nihtianova, D.; Wegner, S.; Tzvetkova, P.; Simova, S. High-voltage $LiNi_{1/2}Mn_{3/2}O_4$ spinel: cationic order and particle size distribution. *J. Phys. Chem. C* **2011**, 115, 25170–25182.

(34) Wang, D. H.; Wang, L. F.; Liang, G. J.; Li, H. F.; Liu, Z. X.; Tang, Z. J.; Liang, J. B.; Zhi, C. Y. A superior δ-MnO_2 cathode and a self-healing Zn-δ-MnO_2 battery. *ACS Nano* **2019**, 13, 10643–10652.

(35) Tan, Q. Y.; Li, X. T.; Zhang, B.; Chen, X.; Tian, Y. W.; Wan, H. Z.; Zhang, L. S; Miao, L.; Wang, C.; Gan, Y.; Jiang, J. J.; Wang, Y.; Wang, H. Valence engineering via in situ carbon reduction on octahedron sites Mn_3O_4 for ultra-long cycle life aqueous Zn-ion battery. *Adv. Energy Mater.* **2020**, 10, 2001050.

(36) Luo, D.; Ding, X. K.; Fan, J. M.; Zhang, Z. H.; Liu, P. Z.; Yang, X. H.; Guo, J. J.; Sun, S. H.; Lin, Z. Accurate control of initial Coulombic efficiency for lithium-rich manganese-based layered oxides by surface multicomponent integration. *Angew. Chem. Int. Ed.* **2020**, 132, 23261–23266.

(37) Yang, J. C.; Chen, Y. X.; Li, Y. J.; Xi, X. M.; Zheng, J. C.; Zhu, Y. L.; Xiong, Y. K.; Liu, S. W. Encouraging voltage stability upon long cycling of Li-rich Mn-based cathode materials by Ta–Mo dual doping. *ACS App. Mater. Interfaces* **2021**, 13, 25981–25992.

(38) Liu, S. Y.; Dang, Z. Y.; Liu, D.; Zhang, C. C.; Huang, T.; Yu, A. S. Comparative studies of zirconium doping and coating on $LiNi_{0.6}Co_{0.2}Mn_{0.2}O_2$ cathode material at elevated temperatures. *J. Power Sources* **2018**, 396, 288–296.

(39) Sun, Y.; Zan, L.; Zhang, Y. X. Enhanced electrochemical performances of Li_2MnO_3 cathode materials via adjusting oxygen vacancies content for lithium-ion batteries. *Appl. Surf. Sci.* **2019**, 483, 270–277.

(40) Luo, D.; Ding, X. K.; Hao, X. D.; Xie, H. X.; Cui, J. X.; Liu, P. Z.; Yang, X. H.; Zhang, Z. H.; Guo, J. J.; Sun, S. H.; Lin, Z. Ni/Mn and Al dual concentration-gradients to mitigate voltage decay and capacity fading of Li-rich layered cathodes. *ACS Energy Lett.* **2021**, 6, 2755–2764.

(41) Wen, X. F.; Liang, K.; Tian, L. Y.; Shi, K. Y.; Zheng, J. S. Al_2O_3 coating on $Li_{1.256}Ni_{0.198}Co_{0.082}Mn_{0.689}O_{2.25}$ with spinel-structure interface layer for superior performance lithium ion batteries. *Electrochim. Acta* **2018**, 260, 549–556.

(42) Ding, X. K.; Luo, D.; Cui, J. X.; Xie, H. X.; Ren, Q. Q.; Lin, Z. An ultra-long-life lithium-rich $Li_{1.2}Mn_{0.6}Ni_{0.2}O_2$ cathode by three-in-one surface modification for lithium-ion batteries. *Angew. Chem. Int. Ed.* **2020**, 132, 7852–7856.

(43) Li, B. Y.; Li, G. S.; Zhang, D.; Fan, J. M.; Feng, T.; Li, L. P. Understanding de-protonation induced formation of spinel phase in Li-rich layered oxides for improved rate performance. *Chin. J. Struct. Chem.* **2018**, 37, 1723–1736.

(44) Sun, H. H.; Kim, U. H.; Park, J. H.; Park, S. W.; Seo, D. H.; Heller, A.; Mullins, C. B.; Yoon, C. S.; Sun, Y. K. Transition metal-doped Ni-rich layered cathode materials for durable Li-ion batteries. *Nat. Commun.* **2021**, 12, 1–11.

(45) Su, Y. F.; Yang, Y. Q.; Chen, L.; Lu, Y.; Bao, L. Y.; Chen, G.; Yang, Z. R.; Zhang, Q. Y.; Wang, J.; Chen, R. J.; Chen, S.; Wu, F. Improving the cycling stability of Ni-rich cathode materials by fabricating surface rock salt phase. *Electrochim. Acta* **2018**, 292, 217–226.

(46) Li, X.; Qiao, Y.; Guo, S. H.; Xu, Z. M.; Zhu, H.; Zhang, X. Y.; Yuan, Y.; He, P.; Ishida, M.; Zhou, H. S. Direct visualization of the reversible O^{2-}/O^{-} redox process in Li-rich cathode materials. *Adv. Mater.* **2018**, 30, 1705197.

(47) Zheng, H. F.; Zhang, C. Y.; Zhang, Y. G.; Lin, L.; Liu, P. F.; Wang, L. S.; Wei, Q. L.; Lin, J.; Sa, B. S.; Xie, Q. S.; Peng, D. L. Manipulating the local electronic structure in Li-rich layered cathode towards superior electrochemical performance. *Adv. Funct. Mater.* **2021**, 31, 2100783.

(48) Luo, D.; Fang, S. H.; Tian, Q. H.; Qu, L.; Yang, L.; Hirano, S. I. Discovery of a surface protective layer: a new insight into countering capacity and voltage degradation for high-energy lithium-ion batteries. *Nano Energy* **2016**, 21, 198–208.

(49) Zang, Y.; Ding, C. X.; Wang, X. C.; Wen, Z. Y.; Chen, C. H. Molybdenum-doped lithium-rich layered-structured cathode material $Li_{1.2}Ni_{0.2}Mn_{0.6}O_2$ with high specific capacity and improved rate performance. *Electrochim. Acta* **2015**, 168, 234–239.

(50) Song, J. H.; Kapylou, A.; Choi, H. S.; Yu, B. Y.; Matulevich, E.; Kang, S. H. Suppression of irreversible capacity loss in Li-rich layered oxide by fluorine doping. *J. Power Sources* **2016**, 313, 65–72.

(51) Weppner, W.; Huggins, R. A. Determination of the kinetic parameters of mixed-conducting electrodes and application to the system Li_3Sb. *J. Electrochem. Soc.* **1977**, 124, 1569–1578.

(52) Yu, C. Y.; Dong, L.; Zhang, Y. X.; Du, K.; Gao, M. M.; Zhao, H. L.; Bai, Y. Promoting electrochemical performances of $LiNi_{0.5}Mn_{1.5}O_4$ cathode via YF_3 surface coating. *Solid State Ion.* **2020**, 357, 115464.

Received: March 21, 2022
Accepted: April 4, 2022
Published: April 8, 2022

DOI: 10.14102/j.cnki.0254-5861.2022-0066